IEEE Trans Med Imaging. Author manuscript; available in PMC 2016 November 01.

Published in final edited form as:
IEEE Trans Med Imaging. 2015 November ; 34(11): 2220–2232. doi:10.1109/TMI.2015.2427236.

Theoretical Investigation of Random Noise-Limited Signal-to-Noise Ratio in MR-based Electrical Properties Tomography

Seung-Kyun Lee, **Selaka Bulumulla**, and **Ileana Hancu**
GE Global Research Center, 1 Research Circle, Niskayuna, NY 12309

Abstract

In magnetic resonance imaging-based electrical properties tomography (MREPT), tissue electrical properties (EPs) are derived from the spatial variation of the transmit RF field (B_1^+). Here we derive theoretically the relationship between the signal-to-noise ratio (SNR) of the electrical properties obtained by MREPT and the SNR of the input B_1^+ data, under the assumption that that latter is much greater than unity, and the noise in B_1^+ at different voxels is statistically independent. It is shown that for a given B_1^+ data, the SNR of both electrical conductivity and relative permittivity is proportional to the square of the linear dimension of the region of interest (ROI) over which the EPs are determined, and to the square root of the number of voxels in the ROI. The relationship also shows how the SNR varies with the main magnetic field (B_0) strength. The predicted SNR is verified through numerical simulations on a cylindrical phantom with an analytically calculated B_1^+ map, and is found to provide explanation of certain aspects of previous experimental results in literature. Our SNR formula can be used to estimate minimum input data SNR and ROI size required to obtain tissue EP maps of desired quality.

Keywords

MRI; MREPT; electrical property; signal-to-noise ratio

Introduction

MR-based electrical properties tomography (MREPT), in its most widely used form, utilizes the Laplacian of the complex transmit RF field (B_1^+) to estimate the electrical conductivity (σ) and relative permittivity (ϵ_r) of tissue in a region of interest (ROI) with constant electrical properties (EPs) [1-4]. Inside biological tissue and at clinical MRI frequencies, the length scale of RF field variation, defined by its wavelength or the skin depth, is on the order of a centimeter to tens of centimeters. When the measured map of such field contains random noise varying over the length scale of a single voxel, high-pass filtering characteristic of Laplacian operation makes accurate determination of true RF field variation difficult. Therefore, signal averaging is often performed either over time to increase the raw data SNR, or over an ROI to spatially average the noise in the Laplacian as much as possible. Knowing the quantitative relationship between the SNR of EPs, raw data SNR, and the ROI size will help determine the experimental conditions necessary to achieve the quality of EP maps desired for a given application. For example, Hancu et al [5] have reported that the difference in relative permittivity between normal tissue and tumor in a mouse model was 27% at 1.5 T. In order to use MREPT for tumor discrimination, therefore, SNR in permittivity greater than 4 is desired. At present, little is published on how this SNR requirement relates to the RF field map SNR. A main goal of this work is to investigate such relationship to inform experimental design regarding SNR and spatial resolution of MR signal acquisition in MREPT experiments.

With the assumption that the primary source of uncertainty in MREPT comes from the Laplacian calculation on a noisy field map (namely, ignoring systematic errors involved in a particular MREPT method), we derive a quantitative relationship between the uncertainties of the raw data and those of the resulting EPs. We start from general, qualitative considerations on what physical factors should affect the EP uncertainty, and how the latter should functionally depend on such factors. Then we take a concrete example of a spherical ROI and demonstrate derivation of a formula relating the input and the output uncertainties. We demonstrate numerical simulations based on an analytical RF solution in a cylindrical phantom with synthetic random noise to verify the derived formula. Implications of the results on the choice of the field strength in MREPT will be discussed.

Several previous works [6-8] have discussed random noise in MREPT. These works have empirically demonstrated how the SNR of the reconstructed EPs vary with the main field strength [7] and the reconstruction methods [6, 8], providing a good benchmark to test any comprehensive MREPT noise theory. We will compare the SNR behaviors reported in these works with the predictions of our theory.

Theory

1. General considerations and assumptions

EPT equation—Suppose that through appropriate methods and approximations we have obtained the complex B_1^+ map in the tissue and we calculate the electrical properties using the known MREPT equations based on the homogeneous Helmholtz equation [1]:

$$\nabla^2 B_1^+ = -k^2 B_1^+ \quad (1)$$

$$k^2 = \omega^2 \epsilon_r \epsilon_0 \mu_0 - i\omega\sigma\mu_0. \quad (2)$$

Here ϵ_0, μ_0 are the permittivity and permeability in vacuum, respectively. The MRI resonance frequency, $\omega = 2\pi f$, is related to the main magnetic field B_0 by $\omega = \gamma B_0$, where $\gamma = 2\pi \cdot 42.578$ MHz/T is the gyromagnetic ratio of ^{1}H in water. Here we assume that B_1^+ is the input data from which EPs are calculated; however, the results obtained in the following are directly transferrable to cases in which quantities other than B_1^+ are used in MREPT. For example, Eqs. (1,2) are applicable to each Cartesian component of $\vec{B}_1$, and the receiver sensitivity field [9]. Also, in the image-based method of [10], $\sqrt{B_1^+ B_1^-}$ replaces B_1^+.

Because of the spatial derivative operation, Eqs. (1,2) need to be applied to a region containing multiple voxels. We will define such a set of voxels a region of interest (ROI); an ROI is a region in which a single ϵ_r and a single σ are determined from MREPT. Unless otherwise noted, in this work we will assume that an ROI is three-dimensional. The ROI should be distinguished from a bigger region or an anatomy (e.g., brain) in which a *map* of EPs is calculated. In the latter case, we will assume that a map is obtained by sweeping the ROI inside the bigger, anatomical region.

Because Eqs. (1,2) are valid for spatially constant ϵ_r and σ, the following analysis is only strictly valid in a homogeneous region with constant EPs. If an ROI contains voxels with non-constant EPs, the resulting error in the reconstructed EPs can surpass the error due to the random noise considered in this work. This is particularly the case if the ROI crosses a tissue boundary. We emphasize that the theoretical validity of our SNR analysis below is limited to cases where the EPs vary sufficiently slowly in an ROI that the SNR of MREPT is limited by the random noise.

Linear Laplacian estimator—For a given ROI, Eq. (1) suggests that k^2 be computed from the ratio between an estimator of the Laplacian of B_1^+ and an estimator of B_1^+ within the ROI, namely,

$$k^2 = -\frac{estimator\left(\nabla^2 B_1^+\right)}{estimator\left(B_1^+\right)}. \quad (3)$$

In this work, we consider a class of methods in which the Laplacian estimator takes a form of the inner product between B_1^+ and a predefined kernel,

$$estimator\left(\nabla^2 B_1^+\right) = \left\langle B_1^+ \right\rangle_g \equiv \sum_{v \in ROI} B_{1,v}^+ \quad g_v. \quad (4)$$

Here $v = 1, 2, \cdots, N_{tot}$ is a voxel index in an ROI containing N_{tot} voxels and g_v, called “Laplacian kernel”, is a set of real numbers that produce a Laplacian estimator of B_1^+ when an inner product is taken with B_1^+.

The estimator of B_1^+ can be defined simply as

$$estimator\left(B_1^+\right) = \left\langle B_1^+ \right\rangle \equiv \frac{1}{N_{tot}} \sum_{v \in ROI} B_{1,v}^+. \quad (5)$$

Although other definitions are possible, for example, a weighted average, our results are not sensitive to the exact definition of the B_1^+ estimator. What is important is that the latter is a quantity independent of the voxel index v. Using Eqs. (4,5), Eq. (3) can be written as

$$k^2 = -\frac{\left\langle B_1^+ \right\rangle_g}{\left\langle B_1^+ \right\rangle}. \quad (6)$$

We note that estimating the Laplacian from a linear kernel includes many published methods of numerical Laplacian computation. For example, finite difference calculation [11], calculation using a special kernel of [12], and an integral method [6, 13] are all a form of linear Laplacian estimation with an appropriately defined kernel. Furthermore, a linear filter applied to the B_1^+ map can be included in the definition of g_v. On the other hand, we are not considering in this work methods involving non-linear filtering.

The electrical properties are obtained from Eqs. (2,6) as

$$\epsilon_r = -\frac{1}{\omega^2\epsilon_0\mu_0} Re\left(\frac{\left\langle B_1^+\right\rangle_g}{\left\langle B_1^+\right\rangle}\right) \quad (7)$$

$$\sigma = \frac{1}{\omega\mu_0} Im\left(\frac{\left\langle B_1^+\right\rangle_g}{\left\langle B_1^+\right\rangle}\right). \quad (8)$$

Noise propagation—Uncertainties in $\in_r$ and σ come from the noise in the B_1^+ map. Qualitatively, if the B_1^+ map has a certain SNR, its ROI average $\left\langle B_1^+\right\rangle$ has a higher SNR by a factor $N_{tot}^{1/2}$. As we generally consider ROI with $N_{tot} >> 1$, one can say that the denominator on the right hand side of Eqs. (7,8) can be determined with relatively high accuracy; uncertainties in $\in_r$ and σ are therefore dominated by the uncertainty in the Laplacian estimator of B_1^+. Our task in this and the following sections is to determine how this uncertainty relates to the SNR of B_1^+. Since we are dealing with the SNR of complex quantities, below we detail our assumptions made on the B_1^+ noise in order to prevent any confusion regarding its definition.

In most MREPT acquisitions, the magnitude and phase of B_1^+ are separately acquired. In such a case, we may assume that the noise in $|B_1^+|$ and the noise in $\angle B_1^+$ are statistically independent. We will further assume that the noise in B_1^+ (magnitude or phase) at different voxels is independent from one another. Lastly we will assume that the magnitude and phase noise is characterized by voxel-independent standard deviation, $\Delta|B_1^+|$ and $\Delta\angle B_1^+$, respectively. Note that here and in what follows Δ() represents statistical uncertainty over repeated trials, and not voxel-to-voxel variation in an ROI (because voxel-to-voxel variation includes true spatial variation of B_1^+). In order to express the uncertainties in $\in_r$ and σ in terms of $\Delta|B_1^+|$ and $\Delta\angle B_1^+$, we now proceed as the following.

First, we rewrite Eqs. (7,8) as

$$\epsilon_r = -\frac{1}{\omega^2\epsilon_0\mu_0} Re\left\langle \frac{B_1^+}{\left\langle B_1^+\right\rangle}\right\rangle_g = -\frac{1}{\omega^2\epsilon_0\mu_0}\left\langle Re\left(\frac{B_1^+}{\left\langle B_1^+\right\rangle}\right)\right\rangle_g \quad (9)$$

$$\sigma = \frac{1}{\omega\mu_0} Im\left\langle \frac{B_1^+}{\left\langle B_1^+\right\rangle}\right\rangle_g = \frac{1}{\omega\mu_0}\left\langle Im\left(\frac{B_1^+}{\left\langle B_1^+\right\rangle}\right)\right\rangle_g. \quad (10)$$

This was done in two steps. (i) $\left\langle B_1^+\right\rangle$, a voxel-independent quantity, can be put inside the Laplacian estimator $\langle\ \rangle_g$. (ii) Since the kernel g is real, the operations of taking an inner product with g and taking the real (or imaginary) parts can be swapped in order.

Eqs. (9,10) show that the EPs are determined by the Laplacian estimator ($\langle\ \rangle_g$) of the real and imaginary parts of the *normalized* B_1^+ map, $B_1^+/\left\langle B_1^+\right\rangle$. Let us denote these quantities as

$$b_r \equiv Re\left(\frac{B_1^+}{\left\langle B_1^+\right\rangle}\right) \quad (11)$$

$$b_i \equiv Im\left(\frac{B_1^+}{\left\langle B_1^+\right\rangle}\right). \quad (12)$$

The uncertainties in ϵ_r and σ are now expressible as

$$\Delta\epsilon_r = \frac{1}{\omega^2\epsilon_0\mu_0}\cdot\Delta\langle b_r\rangle_g \quad (13)$$

$$\Delta\sigma = \frac{1}{\omega\mu_0}\cdot\Delta\langle b_i\rangle_g. \quad (14)$$

In Appendix 1, we show that under realistic conditions, the uncertainties in b_r and b_i themselves are related to the B_1^+ noise by

$$\Delta b_r \approx \frac{1}{SNR_{|B_1^+|}} \quad (15)$$

$$\Delta b_i \approx \Delta\angle B_1^+ \equiv \frac{1}{SNR_{\angle B_1^+}} \quad (16)$$

where $SNR_{|B_1^+|}$ and $SNR_{\angle B_1^+}$ are the B_1^+ map magnitude SNR and the phase SNR in the ROI, respectively. Our next task, therefore, is to determine how the uncertainties in b_r and b_i propagate into the uncertainties in their Laplacian estimators, $\langle b_r \rangle_g$ and $\langle b_i \rangle_g$. This deals with the question of noise amplification by the Laplacian operation.

2. Uncertainty in the Laplacian of noisy data

2.1. Scaling relation

For notational simplicity let us denote either b_r or b_i by a generic real-valued map b. b is defined in an ROI and has a (additive) random real noise at any given voxel in the ROI with standard deviation Δb. For a given realization of b, we evaluate its Laplacian estimator $\langle b \rangle_g$ over the ROI. The estimator statistically varies and its standard deviation, $\Delta \langle b \rangle_g$, is what we seek.

Without knowledge of the specific Laplacian kernel g, we first attempt to come up with a general functional form of $\Delta \langle b \rangle_g$ expressed in terms of a few factors that are expected to affect $\Delta \langle b \rangle_g$. They are the input noise Δb, the number of voxels N_{tot}, and the size of the ROI. First, given that the Laplacian estimator is linear, its standard deviation should be proportional to the input standard deviation: $\Delta \langle b \rangle_g \propto \Delta b$. Second, other factors being equal, the statistical fluctuation of the Laplacian estimator is expected to decrease as the number of independent voxels increases. A reasonable guess for the scaling can be $\Delta \langle b \rangle_g \propto 1/N_{tot}^{1/2}$. Lastly, the physical unit (dimension) of $\Delta \langle b \rangle_g$ is the same as that of $\langle b \rangle_g$, and the latter, being a Laplacian of b, must possess a unit: (unit of b)/(length)^2. One quantity in the problem that has the unit of length is the size of the ROI, which we will denote as L. Whereas the exact definition of L is not important for the discussion in this section, for specificity we define L as the diameter of the smallest sphere that contains the ROI. Without knowing what other length scales (such as ones defined by the input data b) may affect $\Delta \langle b \rangle_g$, we proceed to write $\Delta \langle b \rangle_g$ formally as

$$\Delta \langle b \rangle_g = G \quad \Delta b \quad L^{-2} N_{tot}^{-1/2}. \quad (17)$$

Thanks to having separated out L^{-2}, we can say in the above equation that G is a dimensionless quantity. Eq. (17) can be viewed as the definition of G, as a factor that accounts for any remaining functional dependence of $\Delta \langle b \rangle_g$ after separating out $L^{-2} N_{tot}^{-1/2}$. Its usefulness hinges on whether G still depends on L, N_{tot}, or the input data b. In the following section we will show that G is independent of b when the Laplacian kernel g is noise-optimized (defined below). The usefulness of Eq. (17) will be more apparent as we consider concrete examples.

For now let us use Eq. (17) to replace $\Delta\langle b_r\rangle_g$ in Eq. (13), and $\Delta\langle b_i\rangle_g$ in Eq. (14). In doing so, we also replace the generic input noise Δb by the corresponding noise Δb_r and Δb_i from Eqs. (15,16).

$$\Delta\epsilon_r = G\frac{1}{\omega^2\epsilon_0\mu_0}\cdot\frac{1}{SNR_{|B_1^+|}}\cdot\frac{1}{L^2N_{tot}^{1/2}} \quad (18)$$

$$\Delta\sigma = G\frac{1}{\omega\mu_0}\cdot\Delta\angle B_1^+\cdot\frac{1}{L^2N_{tot}^{1/2}}. \quad (19)$$

The above equations point us to the desired relationship between the EP uncertainties and the raw data SNR and the ROI size. Now let us look in more details into computing G.

2.2. Minimum uncertainty Laplacian estimator

We start by the definition of the Laplacian estimator Eq. (4),

$$\langle b\rangle_g = \sum_{v\in ROI} b_v g_v = \mathbf{b}\cdot\mathbf{g}. \quad (20)$$

Here the bold face symbols indicate row vectors of the corresponding quantities defined on all voxels in the ROI: $\mathbf{b} = (b_1, b_2, \cdots, b_{Ntot})$, $\mathbf{g} = (g_1, g_2, \cdots, g_{Ntot})$.

When b has voxel-independent noise $\Delta b_v = \Delta b$, the noise in Eq. (20) is given by

$$\Delta\langle b\rangle_g = \Delta\sum_v b_v g_v = \sqrt{\sum_v (\Delta b_v)^2 g_v^2} = \Delta b\sqrt{\sum_v g_v^2}. \quad (21)$$

Here we used the general relationship, $\Delta(c_1X_1 + c_2X_2) = \sqrt{c_1^2\cdot(\Delta X_1)^2 + c_2^2\cdot(\Delta X_2)^2}$ for independent statistical variables X_1 and X_2. We find that the root sum-of-squares (rss) of the kernel g_v equals the noise propagation factor between the input (b) and the output ($\langle b\rangle_g$) noise. Further calculation requires knowledge of the kernel g_v. We proceed by looking for a Laplacian kernel g_v that minimizes the rss value and therefore Eq. (21) for a given Δb. We call such a kernel as a "minimum uncertainty Laplacian kernel". In order for g_v to be a Laplacian kernel, it must satisfy the following conditions:

(i) If the input data b is a constant or linear, the inner product of $\mathbf{b}$ and $\mathbf{g}$ must vanish.

(ii) If the input data b is purely parabolic, its inner product with $\mathbf{g}$ must produce the exact Laplacian.

Therefore, we define the problem of finding g_v as follows.

Find a real vector $\mathbf{g} = (g_1, g_2, \cdots, g_{Ntot})$ that minimizes the sum of squares

$$S \equiv \mathbf{g}\mathbf{g}^T = \sum_v g_v^2 \quad (22)$$

subject to

$$\sum_v g_v \cdot 1 = \sum_v g_v x_v = \sum_v g_v y_v = \sum_v g_v z_v = \sum_v g_v x_v y_v = \sum_v g_v y_v z_v = \sum_v g_v z_v x_v = 0, \quad (23)$$

$$\sum_v g_v x_v^2 = \sum_v g_v y_v^2 = \sum_v g_v z_v^2 = 2. \quad (24)$$

Here the variables x_v, y_v, z_v are the Cartesian coordinates of the vth voxel.

This can be converted into a problem of unconditional minimization using 10 Lagrange's multipliers corresponding to Eqs. (23,24). In Appendix 2, we show that the solution for g_v is

$$\mathbf{g} = \begin{pmatrix} 0 & 0 & 0 & 0 & 0 & 0 & 0 & 2 & 2 & 2 \end{pmatrix} \left(\mathbf{F}^T\mathbf{F}\right)^{-1} \mathbf{F}^T, \quad (25)$$

from which the corresponding S is

$$S = \mathbf{g}\mathbf{g}^T = \begin{pmatrix} 0 & 0 & 0 & 0 & 0 & 0 & 0 & 2 & 2 & 2 \end{pmatrix} \left(\mathbf{F}^T\mathbf{F}\right)^{-1} \begin{pmatrix} 0 & 0 & 0 & 0 & 0 & 0 & 0 & 2 & 2 & 2 \end{pmatrix}^T. \quad (26)$$

In the above the matrix **F** has a dimension $N_{tot} \times 10$ and is defined as

$$\mathbf{F} \equiv \left(\mathbf{1}^T, \mathbf{x}^T, \mathbf{y}^T, \mathbf{z}^T, (\mathbf{xy})^T, (\mathbf{yz})^T, (\mathbf{zx})^T, \left(\mathbf{x}^2\right)^T, \left(\mathbf{y}^2\right)^T, \left(\mathbf{z}^2\right)^T\right). \quad (27)$$

where the boldface symbols represent row vectors of length N_{tot}, $\mathbf{1} = (1, 1, \cdots, 1)$, $\mathbf{x} = (x_1, x_2, \cdots, x_{Ntot})$, $\mathbf{y} = (y_1, y_2, \cdots, y_{Ntot})$, $\mathbf{z} = (z_1, z_2, \cdots z_{Ntot})$, etc.

Eq. (26) shows that the sum of squares of the optimized **g** is given by 4 times the sum of the nine elements in the 3 × 3 block in the lower right corner of the 10 × 10 matrix $(\mathbf{F}^T\mathbf{F})^{-1}$. Its evaluation depends on the ROI. Comparing Eqs. (17,21,22,26), we find that the previously defined numerical factor G is in fact independent of the input data **b**.

2.3. Relationship with the Savitzky-Golay filter

Interestingly, the minimum uncertainty Laplacian kernel Eq. (25) is the same as the sum of the three second derivative filters obtained by the least-squares polynomial fitting, known as the Savitzky-Golay differentiation filters [14]. While the original method published [14] was for one-dimensional data only, it can be extended to 2D [15] and 3D [16]. In short, least-squares fitting of noisy data, defined on a 3D grid, to a second order polynomial is an analytically solvable problem. If the data is rearranged in a row vector **b**, then the problem is to solve the linear equation $\mathbf{Fc} = \mathbf{b}^T$ in the least squares sense, where **F** of Eq. (27) defines the polynomials and **c** is the (column) vector of polynomial coefficients. The solution involves the pseudo-inverse matrix of **F**, $\mathbf{c} = (\mathbf{F}^T\mathbf{F})^{-1}\mathbf{F}^T\mathbf{b}^T$. The coefficient of each polynomial term is, therefore, given by the dot product of **b** and each row of the matrix $(\mathbf{F}^T\mathbf{F})^{-1}\mathbf{F}^T$. Since the latter is independent of the input data, it can be viewed as a linear filter or a kernel that produces the desired polynomial coefficient when projected to the input data. With our definition of **F** (Eq. 27), the last three rows of $(\mathbf{F}^T\mathbf{F})^{-1}\mathbf{F}^T$ correspond to the kernels for the coefficients of the terms x^2, y^2, z^2, respectively. If we denote these kernels by $\mathbf{a}_{x^2}^{SG}, \mathbf{a}_{y^2}^{SG}, \mathbf{a}_{z^2}^{SG}$, we can define a Savitzky-Golay Laplacian kernel $\mathbf{g}^{SG}$ as

$$\mathbf{g}^{SG} \equiv 2\mathbf{a}_{x^2}^{SG} + 2\mathbf{a}_{y^2}^{SG} + 2\mathbf{a}_{z^2}^{SG}. \quad (28)$$

Comparing Eq. (25) and Eq. (28), it follows that

$$\mathbf{g}^{SG} = \mathbf{g}. \quad (29)$$

In our opinion, it is not obvious why the kernel $\mathbf{g}^{SG}$ defined in Eq. (28) should also be the minimum uncertainty Laplacian kernel defined in the previous section. The Savitzky-Golay differentiation filters are a set of numbers which, when an inner product is taken with the input data, produce coefficients of polynomial terms that best fit the data, minimizing the mean square *error* between the data and the polynomial. On the other hand, the defining requirement of the minimum uncertainty Laplacian kernel is that the mean square of the *kernel itself* is minimized. To our understanding, Eq. (29) appears non-trivial.

2.4. Relationship with Laplacian estimation through quadratic fitting

From the definition of the Savitzky-Golay filter, Laplacian estimation using the kernel $\mathbf{g}^{SG}$ is mathematically equivalent to calculating the Laplacian through quadratic least-squares fitting to the input data. The advantage of fitting over the finite-difference Laplacian calculation was demonstrated by Katscher et al. [17], where the authors locally fit a “3D parabola” to B_1^+ phase data for breast conductivity mapping. Whereas ref. [17] focused on the advantages in terms of boundary artifact reduction, our work shows that in fact 3D least-squares fitting is theoretically the best linear method to estimate the Laplacian in terms of suppressing noise amplification. We note that a variant to the method is to fit the B_1^+ data along only the three Cartesian directions [18]. Whereas the latter may be computationally faster and may have similar artifact reduction advantages as described in [17], it is expected to be less accurate as voxels outside the three lines are not utilized.

The 3D quadratic fitting method can be generalized by including higher order terms, such as x^3, in the fitting polynomial. Including higher order terms can better separate true second-order spatial variation (Laplacian) from higher order ones when the ROI is large and the underlying (noise-free) B_1^+ map varies rapidly in space. Such extension corresponds to including higher order terms in the definition of **F** in Eq. (27), and is computationally straightforward to implement. An interpretation of the resulting *n*th order Savitzky-Golay Laplacian kernel would be the following: the kernel estimates the Laplacian of noisy data with the minimum statistical uncertainty among all linear kernels that extract the Laplacian from an input data containing spatial variations of up to the *n*th order. We add that for a small ROI in which B_1^+ varies relatively slowly, a situation commonly encountered in MREPT, including higher order terms in Laplacian calculation is not expected to make much difference.

2.5. Solution in the continuous limit

Closed analytical expressions for the kernel g_v and the factor G (Eq. 17) can be found in the continuous limit ($N_{tot}/L \to \infty$) for simple ROI shapes. In this section we demonstrate results for a spherical ROI.

Assume an ROI defined by

$$x^2+y^2+z^2 \leq R^2=(L/2)^2 \quad (30)$$

where L = 2R is the diameter of the sphere. We assume that N_{tot} is so large that summation over the voxels in the ROI can be replaced by a continuous integral over the sphere, scaled by the voxel volume V_{ROI}/N_{tot}. For example, the (2,2) element of the matrix $\mathbf{F}^T\mathbf{F}$ is

$$\begin{aligned}\mathbf{x}\cdot\mathbf{x} \quad &=\sum_v x_v \cdot_v = \frac{N_{tot}}{V_{ROI}}\int_{ROI} x^2 dv \\ &=\frac{N_{tot}}{V_{ROI}}\int_{r=0}^{R}\int_{\theta=0}^{\pi}\int_{\phi=0}^{2\pi}(r\, sin\, cos\, \phi)^2 \cdot r^2\, sin\,\theta\, dr d\theta d\phi \\ &=N_{tot}\frac{3}{4\pi R^3}\cdot\frac{4\pi R^5}{15}=\frac{N_{tot}R^2}{5}.\end{aligned} \quad (31)$$

Thanks to the symmetry of the ROI shape, most of the off-diagonal terms in the matrix are zero and $\mathbf{F}^T\mathbf{F}$ is block-diagonal. It turns out that the terms corresponding to 1, x^2, y^2, z^2 do not mix with the other terms. As a result Eq. (25) can be simplified as

$$\mathbf{g}=\begin{pmatrix} 0 & 2 & 2 & 2 \end{pmatrix}\begin{pmatrix} \mathbf{1}\cdot\mathbf{1} & \mathbf{x}^2\cdot\mathbf{1} & \mathbf{y}^2\cdot\mathbf{1} & \mathbf{z}^2\cdot\mathbf{1} \\ \mathbf{1}\cdot\mathbf{x^2} & \mathbf{x}^2\cdot\mathbf{x}^2 & \mathbf{y}^2\cdot\mathbf{x}^2 & \mathbf{z}^2\cdot\mathbf{x}^2 \\ \mathbf{1}\cdot\mathbf{y^2} & \mathbf{x}^2\cdot\mathbf{y}^2 & \mathbf{y}^2\cdot\mathbf{y}^2 & \mathbf{z}^2\cdot\mathbf{y}^2 \\ \mathbf{1}\cdot\mathbf{z} & \mathbf{x}^2\cdot\mathbf{z}^2 & \mathbf{y}^2\cdot\mathbf{z}^2 & \mathbf{z}^2\cdot\mathbf{z}^2 \end{pmatrix}^{-1}\begin{pmatrix} \mathbf{1} \\ \mathbf{x}^2 \\ \mathbf{y}^2 \\ \mathbf{z}^2 \end{pmatrix}. \quad (32)$$

If we call the 4 by 4 matrix in the middle of the right hand side of the above equation as α^{-1}, the elements of α can be calculated through definite integrals similar to Eq. (31):

$$\mathbf{x}^2\cdot\mathbf{1}=\mathbf{y^2}\cdot\mathbf{1}=\mathbf{z^2}\cdot\mathbf{1}=\mathbf{N_{tot}}\quad \mathbf{R^2/5} \quad (33)$$

$$\mathbf{x}^2\cdot\mathbf{x}^2=\mathbf{y}^2\cdot\mathbf{y}^2=\mathbf{z}^2\cdot\mathbf{z}^2=N_{tot}\quad 3R^4/35 \quad (34)$$

$$\mathbf{x}^2\cdot\mathbf{y}^2=\mathbf{y}^2\cdot\mathbf{z}^2=\mathbf{z}^2\cdot\mathbf{x}^2=N_{tot}\quad R^4/35. \quad (35)$$

Note that the first (1, 1) element of α is $\mathbf{1}\cdot\mathbf{1}=\mathbf{\Sigma_v}\quad \mathbf{1}\cdot\mathbf{1}=\mathbf{N_{tot}}$.

The inversion of α can be done explicitly,

$$\boldsymbol{\alpha}^{-1}=\frac{5}{4\quad N_{tot}}\begin{pmatrix} 5 & -7/R^2 & -7/R^2 & -7/R^2 \\ -7/R^2 & 21/R^4 & 7/R^4 & 7/R^4 \\ -7/R^2 & 7/R^4 & 21/R^4 & 7/R^4 \\ -7/R^2 & 7/R^4 & 7/R^4 & 21/R^4 \end{pmatrix} \quad (36)$$

from which we get the desired kernel,

$$\mathbf{g}=\begin{pmatrix} 0 & 2 & 2 & 2 \end{pmatrix} \quad \boldsymbol{\alpha}^{-1}\begin{pmatrix} \mathbf{1} \\ \mathbf{x}^2 \\ \mathbf{y}^2 \\ \mathbf{z}^2 \end{pmatrix}=\frac{35}{2N_{tot}R^4}\left(-3R^2\mathbf{1}+\mathbf{5}\left(\mathbf{x^2}+\mathbf{y^2}+\mathbf{z^2}\right)\right). \quad (37)$$

The sum of squares of the kernel is four times the sum of the nine elements of the 3 by 3 block in the lower right corner of α^{-1} ,

$$S=\mathbf{g}\mathbf{g}^T=4\cdot\frac{5}{4N_{tot}}\cdot\frac{3\cdot5\cdot7}{R^4}=\frac{20^2\cdot21}{N_{tot}L^4} \quad (38)$$

where we used $R = L/2$.

Combining Eqs. (21, 22, 38), we conclude that for a spherical ROI of diameter L, the Laplacian uncertainty is

$$\Delta\langle b\rangle_g=\Delta b\frac{1}{\sqrt{N_{tot}}}\frac{1}{L^2}20\sqrt{21}. \quad (39)$$

Comparing Eq. (39) with Eq. (17), we obtain G for a spherical ROI,

$$G=20\sqrt{21}\approx 91.65. \quad (40)$$

In the above derivation the shape of the ROI enters the process only during calculation of the matrix elements such as Eq. (31), and the process can easily be extended to general ROI shapes. Before turning to discrete grid examples ($_{tot}$ not being very large), we summarize in Table 1 and Fig. 1 results for a 2D circular ROI (defined by $x^2 + y^2 \le (L/2)^2$) and a 1D linear ROI (defined by $|x|<L/2$). From these analytically solvable cases we observe the following:

(1) Eq. (17) provides a valid scaling relationship between $\Delta\langle b\rangle_g$, N_{tot}, and L regardless of the ROI's dimensionality.

(2) If we fix the voxel size in the ROI, the number of voxels scales as $N_{tot} \propto L^d$, where d = 1,2,3 is the ROI's dimensionality. Then Eq. (17) implies that the Laplacian uncertainty scales with L as $\Delta\langle b\rangle_g \propto L^{-2-d/2}$. Therefore the higher d, the more rapidly the Laplacian uncertainty decreases with growing ROI size. For d = 3, the scaling goes as $L^{-3.5}$.

(3) The minimum uncertainty Laplacian kernel is a smooth function of the coordinates which tends to be negative in the center and positive at the boundary of the ROI. This is reminiscent of a generic second derivative "kernel", (1, −2 , 1), and the original 1D Savitzky-Golay 2nd order differentiation filters [14].

2.6. Minimum uncertainty Laplacian kernel on a discrete lattice

The process of constructing the minimum uncertainty Laplacian kernel from a discrete ROI mask follows the general steps of constructing a Savitzky-Golay kernel through the least squares polynomial fitting.

(1) Assign Cartesian coordinates to each voxel in the mask. The origin of the coordinates can be assigned to a point in the approximate center of the ROI.

(2) Form a matrix **F** out of column vectors of unity (**1**), quadratic ($\mathbf{x}^2, \mathbf{y}^2, \mathbf{z}^2$), linear (**x, y, z**) and cross (**xy, yz, zx**) terms. For a symmetric ROI with mirror symmetries in all three directions (such as a sphere or a cuboid), both linear and cross terms can be omitted. This is because for such an ROI, the inner product of an even-parity term (unity and quadratic) and an odd-parity term (linear and cross) vanishes. This causes the matrix $\mathbf{F}^T\mathbf{F}$ to be block-diagonal to allow **g** to be calculated with a reduced matrix, as in Eq. (32). In this case **F** with a size $N_{tot} \times 4$, constructed from only the constant and quadratic terms, will suffice. Otherwise, **F** will generally have a size $N_{tot} \times 10$. Let's say the number of polynomial terms is N_{terms}.

(3) Calculate a $N_{terms} \times N_{tot}$ matrix **A** according to

$$\mathbf{A} \equiv \left(\mathbf{F}^T\mathbf{F}\right)^{-1}\mathbf{F}^T. \quad (41)$$

Each row of **A** represents the Savitzky-Golay kernel for the coefficient of the corresponding polynomial term.

(4) The Laplacian kernel is given by twice the sum of the three rows of **A** that correspond to $\mathbf{x}^2, \mathbf{y}^2, \mathbf{z}^2$.

(5) Final answer is given by rearranging the Laplacian kernel into a grid matching the ROI's shape.

Figure 2 compares three Laplacian kernels constructed for the same ROI shown in Fig. 2(d). This ROI mask fits in a grid of size 7 × 7 × 5, and is taken from the Laplacian kernel used in van Lier et al [12]. Uniform voxel spacing (=1) is assumed. The three kernels shown are:

(a) *Averaged nearest-neighbor kernel K_{nn}*—A nearest-neighbor Laplacian at a single voxel is defined by adding the six nearest neighbor voxels and subtracting six times the center voxel. If there are N_{nn} voxels in the ROI at which such Laplacian can be defined without crossing the ROI boundary, there can be constructed N_{nn} independent Laplacian kernels in the ROI. Adding them up and dividing by N_{nn} defines K_{nn}.

(b) *van Lier's kernel K_{vL}*—The three kernels listed in [12] for the second derivatives in the three Cartesian directions were added up and scaled to satisfy Eqs. (23-24).

(c) *Savitzky-Golay kernel K_{SG}*—This was obtained by the steps (1-5) described above applied to this particular ROI.

All three kernels are scaled so that they satisfy the requirements Eqs. (23-24). At the top of each figure, the rss value of the kernel and the number of non-zero voxels in the kernel are displayed. Figure 2 shows that K_{SG} indeed has the smallest rss value. K_{nn} has about 2.5 times larger rss value, which translates into 2.5 times higher Laplacian noise amplification compared to K_{SG}. The rss value and noise amplification of K_{vL} are in between those of K_{nn} and K_{SG}.

A few notes are in order regarding K_{nn}. K_{nn} estimates the Laplacian inside an ROI by averaging the voxel-wise nearest neighbor Laplacians. Due to massive cancellation inside the ROI, such estimator becomes mathematically equivalent to summing the nearest neighbor *first-order* derivatives of the input data along the ROI's boundary. The third image of Fig. 2(a) graphically illustrates this point. In the continuous limit, this is expressed using the divergence theorem, $\int_V \nabla^2 f dv = \int_V \nabla \cdot \nabla f \quad dv = \int_{\partial V} \nabla f \cdot \hat{n} da$, which forms the basis of the "integral method" [8, 13]. Therefore, K_{nn} can be viewed as a kernel that represents a form of the integral method. For a given ROI, the integral method generally outperforms a single, unaveraged finite-difference Laplacian formula [8]. For example, if we construct a finite-difference Laplacian kernel from the six voxels on the far faces of the ROI and the central voxel, we can show that its rss value is 1.03, indeed larger than that of K_{nn}. Qualitatively, K_{nn} underperforms K_{vL} and K_{SG} because only voxels near the ROI boundary contribute to the computation. This leads to insufficient noise cancellation which results in a higher level of apparent noise amplification compared to more smoothly varying kernels such as K_{vL} and K_{SG}.

Now let us define L for this ROI as the diameter of the smallest sphere that fits around it, $L = \sqrt{67} = 8.185$. The corresponding G factor for K_{SG} is

$$G_{SG} \equiv rss\left(K_{SG}\right) \cdot N_{tot}^{1/2} \cdot L^2 = 0.2321 \cdot \sqrt{117} \cdot 67 = 168.2. \quad (42)$$

Similarly, we get $G_{vL} = 290.2$ and $G_{nn} = 420.8$. These numbers are significantly larger than the G factor (= 91.65) for a spherical ROI with the same L. The G factor is a function of both the ROI geometry and the exact Laplacian kernel used in that ROI. We have shown in sections 2.2 and 2.3 that for a given ROI, the Savitzky-Golay Laplacian kernel has the lowest G factor. Here we see that when the Savitzky-Golay Laplacian kernel is constructed in a spherical ROI and an ROI of Fig. 2(d), a sphere has a lower G factor.

3. SNR of MREPT

3.1. Relative uncertainty and SNR in electrical properties for a spherical ROI

We now proceed to the main results of this work. For specificity, we assume a Savitzky-Golay Laplacian kernel defined on a spherical ROI with diameter L. The results below can be applied to other ROIs and kernels by changing the factor 20√21 to the corresponding G factor. We divide Eqs. (18,19) by ϵ_r and σ, respectively, and use Eq. (2) to replace $\omega^2 \epsilon_r \epsilon_0 \mu_0$ by $Re(k^2)$ and $\omega\sigma\mu_0$ by $|Im\left(k^2\right)|$. Substituting G = 20√21 (Eq. (40)) we get the following results.

$$\frac{\Delta\epsilon_r}{\epsilon_r}=\frac{1}{SNR_{|B_1^+|}}\cdot\frac{1}{\sqrt{N_{tot}}}\cdot\frac{1}{Re\left(k^2\right)L^2}\cdot 20\sqrt{21}, \quad (43)$$

$$\frac{\Delta\sigma}{\sigma}=\Delta\angle B_1^+\cdot\frac{1}{\sqrt{N_{tot}}}\cdot\frac{1}{|Im\left(k^2\right)|L^2}\cdot 20\sqrt{21}. \quad (44)$$

Taking the reciprocal of the above and defining $SNR_{\epsilon_r}\equiv\epsilon_r/\Delta\epsilon_r$, $SNR_\sigma\equiv\sigma/\Delta\sigma$, we get:

$$SNR_{\epsilon_r}=SNR_{|B_1^+|}\cdot\sqrt{N_{tot}}\cdot Re\left(k^2\right)L^2\cdot\frac{1}{20\sqrt{21}}, \quad (45)$$

$$SNR_\sigma=SNR_{\angle B_1^+}\cdot\sqrt{N_{tot}}\cdot|Im\left(k^2\right)|L^2\cdot\frac{1}{20\sqrt{21}}. \quad (46)$$

The SNR of EPs is proportional to the SNR of the B_1^+ map, to the square root of the number of voxels (N_{tot}), to the square of the ROI size (L), and to the magnitude of real or imaginary part of k^2. Given that the real and imaginary parts of k^2 are proportional to 1/(wavelength)^2 and 1/(skin depth)^2 in the tissue, respectively, one can say that the SNR of EP is inversely proportional to the square of the RF length scales (wavelength or skin depth) of the tissue. The numerical factor of 1/G/=1(20√21)=0.0109 is a substantial hit to the SNR. The scaling with (N_{tot}), L, wavelength, skin depth, MRI frequency (through k^2), is the same for different ROI shapes and dimensions. Different shapes of the ROI will affect SNR through change of the G factor.

3.2 MRI field dependence

MRI field (B0) or frequency dependence of the relative uncertainty (SNR) in EPs comes from several sources: frequency dependence of RF length scales (wavelength and skin depth), raw data SNR, and accuracy of any approximations made to the MREPT equations. Eqs. (45,46) provide a way to predict how the SNR in EPs changes with B0 through changes in the RF length scales for a given raw data SNR. Note that the RF length scales depend on the EPs themselves, which also vary with the frequency.

As an example, consider experimental conditions listed in Table 2. We assume a spherical ROI with diameter L = 2 cm. Table 3 shows the SNR in the EPs of the brain tissue (grey and white matter) according to Eqs. (45,46) under the conditions of Table 2. Three MRI fields, 1.5, 3, 7 T were considered. EPs of the brain tissue were obtained from the 4-term Cole-Cole equation [19, 20].

Table 3 shows the advantage of higher MRI frequencies in achieving high SNR in MREPT. For relative permittivity, decrease in $\in r$ with frequency is outweighed by the quadratic factor ω^2 to make $Re(k^2)$, and therefore the $SNR_{\in r}$, grow rapidly with the MRI field strength. For conductivity, increase in both σ and ω with the field makes similarly distinct increase in SNR with the MRI field strength. These results are for a fixed raw data $\left(B_1^+\right)$ SNR. 7T acquisition may provide even greater SNR benefit to MREPT due to higher raw image SNR.

When MREPT is used for additional tissue contrast, contrast-to-noise ratio is important to determine the merit of the method. In ref [5], permittivity contrast between normal tissue and tumor in a rat model increased significantly at lower frequencies. However, rapid decrease in $Re(k^2)$ at lower frequencies, and the resulting loss in $SNR_{\in r}$, will likely make low-frequency permittivity contrast imaging using MREPT difficult.

4. Numerical experiment

4.1 Noise in EP maps and comparison of kernels

All numerical computation was done with Matlab (Mathworks, Natick, MA, USA). The simulation model (phantom) consisted of an infinitely long cylinder with three concentric cylindrical regions labeled I, II, III from the inside out. The outer radii of the regions were 4 cm, 6 cm, and 10 cm. The following EPs were assigned to each region: ($\in_r$, σ) = (80,2.0) for I, ($\in_r$, σ) = (10,0.1) for II, and (($\in_r$, σ) = (80,0.8) for III, in which σ is in [S/m]. Regions I and II roughly mimic a high conductivity lesion (such as tumor) surrounded by fatty tissue. Closed-form analytical solution for the complex B_1^+ map at 128 MHz was obtained following the method of [21] by solving the Maxwell's equations in an axisymmetric geometry with boundary matching.

The phantom was discretized in a grid with voxel size 2 × 2 × 2 mm^3. The axis of the cylinder was defined as the z axis. Gaussian random noise was added to the magnitude and phase of B_1^+, independently, at each voxel. The noise amplitudes were chosen such that $SNR_{|B_1^+|}$ = 330 and $SNR_{\angle B_1^+}$ = 200 at the center of the cylinder's cross section (slice). EP maps on the slice were reconstructed from the synthesized B_1^+ data. First, an ROI mask of Fig. 2(d) was centered on each voxel in the slice. The mask fit in a 7 × 7 × 5 grid, which corresponded to a volume of 1.4 × 1.4 × 1 cm^3. If the ROI mask was fully contained within the outer boundary of the phantom, B_1^+ values in the ROI were processed to calculate EP values according to Eqs. (7,8), and the latter were assigned to the ROI's center voxel. If the ROI mask was not fully contained within the phantom, EP values were not calculated for such voxels. The process was applied blindly across the inner boundaries of the phantom, with no attempt of region segmentation. Three Laplacian kernels defined in Section 2.6 (Fig.

2(a-c)), namely the averaged nearest neighbor (nn) kernel, van Lier's (vL) kernel, and the Savitzky-Golay (SG) kernel, were used for EP calculation and the results were compared.

Figure 3(a) shows the calculated EP maps in comparison with the true EP values of the model. Qualitatively, we observe the following:

(1) The SG kernel produces the lowest noise EP maps among the three kernels, whereas the vL kernel outperforms the nn kernel. This is consistent with the predictions of Section 2.6.

(2) For all three kernels, there are significant boundary artifacts near the two internal “tissue” boundary lines, creating two annular sets of pixels with invalid EP values; the width of the annulus is approximately the size of the ROI.

Figure 3(c) lists the pixel mean, standard deviation, and the SNR of the EP values on different regions of the phantom. In calculating the statistics, we excluded “boundary artifact” pixels for which the ROI centered on them crossed the tissue boundary. We find that the SNR in both $\in_r$ and σ is generally higher in regions with higher values of EPs. For example, the region I, which has the highest conductivity, has the highest SNR in conductivity of all regions for any given Laplacian kernel. On the other hand, the middle (II) region, mimicking fatty tissue with low $\in_r$ and σ, has the poorest SNR for both $\in_r$ and σ. This trend is consistent with the theoretical dependence of the SNR on the RF length scales (e.g. Eqs. (45, 46)); the higher the EP values, the faster the RF field varies in space, which leads to higher EP SNR.

Note that earlier we emphasized the difference between the statistical noise in EPs at a given voxel over many realizations of B_1^+, and voxel-to-voxel EP variation for a given realization of the B_1^+ map. Whereas the former, which was used in the theory section, is different from the latter, which is shown in Fig. 3(a), the two measures are comparable when many voxels with statistically independent B_1^+ noise are present in a homogeneous region. Therefore the observed agreement between the theoretical predictions and the numerical experiment is still relevant.

The left column of Fig. 3(b) shows the SNR of the magnitude and the phase of B_1^+ at each pixel, as used in the numerical model. The random noise added to both the magnitude and the phase of B_1^+ had each a constant statistical amplitude across the pixels. However, the magnitude of the true (i.e., before adding noise) B_1^+ had spatial variation, which caused the spatial variation of $SNR_{|B_1^+|}$. On the other hand, the phase SNR (Eq. (16)) is uniform across the phantom. One merit of our theory is the ability to quantitatively predict the EP SNR based on the B_1^+ SNR. The right column of Fig. 3(b) shows the theoretical SNR of EPs at each pixel according to Eqs. (45,46), in which the factor 20√21 was replaced by the *G* factor (=123) of the SG kernel on the ROI used. Fig. 3(b) indicates that even for very high B_1^+ SNR used in this model, the predicted EP SNR is relatively low, in the range of 3 to 7 for the highest SNR region (I). The theoretical SNR is well reproduced by the results of the numerical experiment, as tabulated in Fig. 3(c).

The numerical study of this section indicates that when a kernel has a relatively small size both in terms of the physical dimension (1.4 cm) and the number of voxels (7 or less along any Cartesian direction), a B_1^+ map with very high SNR is required to achieve a useful SNR in EP mapping. For a given B_1^+ map, the choice of the Laplacian kernel can significantly impact the noise of EP mapping.

4.2. ROI size dependence

Our theory predicts rapid increase of EP SNR with the ROI size. This is demonstrated in Fig. 4. Here the EPs of a numerical cylinder phantom were calculated with the Savitzky-Golay Laplacian kernel defined on a series of ROIs approximating spheres with different diameters, L = 0.2 N_x= [cm], ranging from N_x=5 to 29 (L = 1.0 cm to 5.8 cm). The ($\in_r$, σ) data were synthesized in the same way as in the previous section, except that the cylinder, with 20 cm diameter, was homogeneous with ($\in_r$, σ)=(80, 0.8 S/m). Instead of looking at spatial variation of the reconstructed EPs, we tracked statistical variation of EPs in a given ROI (at the center of the cylinder) over many (1000) runs. The SNR of EPs was defined as the ratio between the standard deviation over the 1000 runs and the true EP values. The SG kernel for a given ROI mask was calculated following the steps of section 2.6. The process was repeated for each ROI diameter. A total of 13 different ROIs and corresponding SG kernels were used in the study. For each ROI, the G factor defined in Eq. (42) was computed and compared with the continuous-limit value 20√21 (Eq. (40)).

Figure 4(a) shows that the simulated SNR of EPs agrees very well with the theoretical SNR obtained by Eqs. (45,46). This also verifies the approximations Eqs. (15,16) which relates the noise in B_1^+ magnitude and phase separately to the noise in the real and imaginary parts of the normalized B_1^+ (Appendix 1). We find that a very poor SNR of between 1 and 2 at L = 1.0 cm (N_x= 5) grows to an SNR > 100 at L = 4.0 cm (N_x = 20). The scaling of SNR with the ROI size follows SNR $\sim N_x^{3.5}$ as predicted (Section 2.5) when only the SNR due to random noise is considered.

Figure 4(b) shows the statistical mean values of the reconstructed EPs in a given ROI as a function of the ROI size. Note that the accuracy of the EP calculation slowly degrades at a large N_x. This is because for a large ROI, higher (>2) order spatial variation of the B_1^+ map becomes significant, and it is not accounted for in the second-order polynomial fitting, which our SG kernel is based on. Including higher order terms in the construction of the SG kernel could reduce this discrepancy for a large ROI.

Figure 4(c) shows that the G factor for a spherical ROI calculated in the continuous limit (Eq. (40)) predicts well the numerical G factors on a discrete grid.

Our theory predicts rapid increase of EP SNR with the ROI size. This is demonstrated in Fig. 4. Here the EPs of a numerical cylinder phantom were calculated with the Savitzky-Golay Laplacian kernel defined on a series of ROIs approximating spheres with different diameters, L = 0.2 N_x [cm], ranging from N_x = 5 to 29 (L = 1.0 cm to 5.8 cm). The B_1^+ data were synthesized in the same way as in the previous section, except that the cylinder, with

20 cm diameter, was homogeneous with (ϵ_r, σ) = (80, 0.8 S/m). Instead of looking at spatial variation of the reconstructed EPs, we tracked statistical variation of EPs in a given ROI (at the center of the cylinder) over many (1000) runs. The SNR of EPs was defined as the ratio between the standard deviation over the 1000 runs and the true EP values. The SG kernel for a given ROI mask was calculated following the steps of section 2.6. The process was repeated for each ROI diameter. A total of 13 different ROIs and corresponding SG kernels were used in the study. For each ROI, the G factor defined in Eq. (42) was computed and compared with the continuous-limit value 20√21 (Eq. (40)).

Figure 4(a) shows that the simulated SNR of EPs agrees very well with the theoretical SNR obtained by Eqs. (45,46). This also verifies the approximations Eqs. (15,16) which relates the noise in B_1^+ magnitude and phase separately to the noise in the real and imaginary parts of the normalized B_1^+ (Appendix 1). We find that a very poor SNR of between 1 and 2 at L = 1.0 cm (N_x=5) grows to an SNR > 100 at L = 4.0 cm (N_x=20). The scaling of SNR with the ROI size follows SNR $\sim N_x^{3.5}$ as predicted (Section 2.5) when only the SNR due to random noise is considered.

Figure 4(b) shows the statistical mean values of the reconstructed EPs in a given ROI as a function of the ROI size. Note that the accuracy of the EP calculation slowly degrades at a large N_x. This is because for a large ROI, higher (>2) order spatial variation of the B_1^+ map becomes significant, and it is not accounted for in the second-order polynomial fitting, which our SG kernel is based on. Including higher order terms in the construction of the SG kernel could reduce this discrepancy for a large ROI.

Figure 4(c) shows that the *G* factor for a spherical ROI calculated in the continuous limit (Eq. (40)) predicts well the numerical *G* factors on a discrete grid.

5. Comparison with previous experimental results

Experimental studies of the behavior of SNR in MREPT have been published earlier. Katscher et al. [6] investigated the SNR of the simulated and measured conductivity as a function of the reconstruction parameters at 1.5 Tesla. The authors noted that the SNR of the reconstructed conductivity was proportional to that of the B1 map, and plotted their ratio for a bi-cylindrical phantom as a function of two reconstruction parameters: the number of pixels ($2I + 1$) used for linear derivative computation and the integration area ($L2$), as relevant in the particular reconstruction equations used (Eqs. (3,4) of [6]). Translated to our formulation, I and L determine the Laplacian kernel shape and its size. Based on the descriptions of ref. [6], we attempted to reproduce the corresponding Laplacian kernels (K) and the predicted SNR ratios. For the kernel K, we assumed the simplest approximation model mentioned in ref. [6], namely $H_z = H^-$=0. Figure 5(b) shows an example. For the SNR ratio, we used our Eq. (46) where the factor $\sqrt{N_{tot}}L^2/(20\sqrt{21})$ was replaced by $1/rss(K)$ (see Eq. (42)). Explicitly, we plotted

$$\frac{SNR_\sigma}{SNR_{\angle B_1^+}} = \frac{|Im(k^2)|}{rss(K)} \quad (47)$$

for a phantom with σ = 2.5 S/m, for which$|Im(k2)| = \omega\sigma\mu_0 = 1263$ [m^{-2}]

Figure 5(a) shows the result. Comparing this with Fig. 5 of ref. [6], we find that the general trend of the SNR ratio is well predicted. A main difference between the two figures is the definition of the SNR ratio on the *y* axis; our theory predicts the SNR ratio with respect to the B_1 phase SNR, whereas in ref. [6] the ratio used the “B_1 map” SNR. If the latter meant the B_1 magnitude SNR, it is conceivable that it was a smaller number than the B_1 phase SNR (which seems to be the case from Fig. 7(d) of ref. [6]). In such a case, the SNR ratio of our prediction should be smaller than that of ref. [6], which is what is observed.

Van Lier et al. [7] have investigated the accuracy and precision of MREPT at 1.5, 3, and 7 Tesla through phantom and in-vivo experiments. We observe the following from the experimental EP maps of [7]:

(1) Random noise in EP maps in the brain and a brain-sized phantom is very high at 1.5 T, to the point where quantification of EPs is severely hampered.

(2) The random noise decreases rapidly as B_0 increases from 1.5 to 7 T.

(3) From visual inspection of the phantom results (Figs. (5,6) of [7]), the noise in permittivity appears to decrease with B_0 more dramatically than the conductivity noise.

These features can be qualitatively explained by our theoretical predictions.

(1) Table 3 shows that at 1.5 T, the EP SNR in brain tissue is generally low, being less than 4 under the conditions of Table 2. The SNR calculation assumed the input (B_1^+) SNR of 100 for both the magnitude and phase, and a noise-minimizing Savitzky-Golay Laplacian kernel on a sphere (G = 91.65) with diameter L = 2.0 cm containing N_{tot}=1000 voxels. On the other hand, ref [7] used a kernel that was an anisotropic version of the kernel K_{vL} (Fig. 2). The largest linear dimension of the kernel in [7] was L = 2.72 cm. If we therefore scale the SNR according to $SNR \propto N_{tot}^{1/2} L^2 / G$ (Eqs. (45,46)), we estimate that the EP SNR of Table 3 is reduced by a factor $\sqrt{1000/117} \cdot (2.0/2.72)^2 \cdot (290.2/91.65) = 5.0$ where the G factor 290.2 was taken from section 2.6. This decreases the theoretical SNR in ϵ_r and σ of grey matter at 1.5 T from 2.4 and 3.5 (Table 3) to 0.48 and 0.7, respectively. Such low SNR will indeed make quantification of EPs difficult.

(2)(3) According to Eqs. (45,46), B_0 increase from 1.5 to 7 T causes increase in SNR in ϵ_r and σ by $(71.5/)^2$=21.8 and 71.5/=4.67, respectively, for a given input (B_1^+) SNR and frequency-independent EPs (as was the case in [7]). Although B_1^+ SNR was not available from ref. [7], it is conceivable that 7 T scans had a higher B_1^+ SNR than 1.5 T scans, which would increase the field-dependent SNR gain to an even higher value. Very large, at least an order-of-magnitude gain in SNR in permittivity at 7 T compared to 1.5 T is apparent in Fig. 6 of ref. [7].

In addition to the qualitative observations, ref. [7] also provides quantitative analysis of the measured noise in the electrical properties. The blue bars in Fig. 7 of [7] indicate the measured "noise level", defined by the standard deviation of the experimental EP maps on a homogeneous compartment of the phantom, normalized by the true EP values. According to this plot, the noise level decreases monotonically with B0; the noise reduction factor from 1.5T to 7T was reported to be 3.1 for permittivity, and 3.8 for conductivity. These numbers are considerably smaller than the predicted gain in random-noise-limited SNR (21.8 for ϵ_r and 4.67 for σ) from our theory. One possible reason for the difference is that the reported noise level in the plot of [7] could have contained contributions from reconstruction errors (due to phase approximation) that are larger for 7T than for 1.5T. Even though the plot separately shows the reconstruction errors (green and red bars) for each field strength, they were taken from a separate simulation study, and it does not appear as if the blue bars were obtained after subtracting such non-random errors. For example, inspection of the three measured permittivity maps in Fig. 6 of [7] strongly suggests that the random noise at 1.5T is at least an order of magnitude larger than at 7T; at 1.5T, many pixels are out of the color range, whereas at 7T, the permittivity variation appears to be more attributable to non-random reconstruction errors. If this had been the case, the actual random noise reduction factor from 1.5T to 7T would have been much higher than 3.1, consistent with our theory.

6. Dicussion

Random noise amplification by Laplacian operation has been known to be a challenge in MREPT that relies on the Laplacian of the measured B_1^+ map. In this work we have quantified the noise amplification by introducing the minimum uncertainty Laplacian kernel, and demonstrating explicit derivation of random noise-limited electrical properties SNR equations for a specific (spherical) kernel shape. Our results showed that the Laplacian noise contains a factor (G) that depends on the kernel shape, as well as factors (L^2, N_{tot}) that depend on the size of the kernel. Further analysis also revealed how the EP uncertainties scale with the complex RF wave number k^2 and through it, with the B_0 strength.

We have elucidated the relationship between the Savitzky-Golay second derivative filter, quadratic fitting, and the minimum uncertainty Laplacian kernel. By explicit derivation, we showed that a Laplacian kernel obtained by the Savitzky-Golay second derivative filters achieve the lowest noise amplification among all linear Laplacian kernels satisfying Eqs. (23,24). We have outlined numerical steps to compute such a kernel (section 2.6) for an arbitrary ROI. This result will be useful for Laplacian estimation in MREPT and in any other applications requiring the Laplacian of noisy data.

An implication of the theoretical EP SNR formula is that EPs calculated from a small ROI suffer a disproportionately large penalty in random noise-limited SNR. In 3D and for a fixed voxel size, the loss in SNR follows the 3.5th order power law with respect to the linear size of the ROI. This implies that dividing a large ROI into smaller ROIs and averaging EPs obtained from the latter can be much less precise than calculating EPs from the original, larger ROI with a matching Laplacian kernel.

In this work we have ignored any correlated noise or systematic errors in MREPT. For example, the predicted benefit of lower uncertainty in MREPT at higher field strengths should be balanced with potential increase in systematic errors [7] due to inaccurate B_1^+ phase assumption, when a single transmit and receive RF coil is used. Phase assumption errors at high fields could be reduced by use of multiple RF coils for transmission and reception [22, 23]. Similarly, it is possible that the increase in EP SNR with the ROI size may be less dramatic than the predicted 3.5th power dependence. This is because our theory (as well as the numerical simulation) assumed that noise in different voxels was uncorrelated. In practice, hardware drift and instabilities can cause inter-voxel noise correlation. For example, in the Weisskoff analysis performed on a 2D image [24], repeated MRI measurements ideally results in fluctuations in the ROI-averaged signal amplitude that decrease linearly with the ROI dimension. In a survey of clinical scanners, however, the radius of decorrelation (RDC), which was a measure of the size of the ROI at which statistical independence of the voxels is lost, was found to range between 4 and 17 voxels [25]. Likewise, past a similarly defined RDC point further increase in the ROI size for EP calculation will reach a point of diminishing returns.

In a heterogeneous medium such as biological tissue, a larger ROI is more likely to include voxels at EP boundaries where the homogeneous Helmholtz equation-based MREPT formulation (Eqs. (1,2)) fails. Boundary artifacts produced by such voxels are apparent in the numerical simulation shown in Fig. 3(a), where the width of the artifact “ring” is set by the ROI size. The proposed Savitzky-Golay kernel may perform relatively poorly near the boundaries compared to other kernels because it tends to weigh heavily distant voxels in the ROI.

Recent works by Liu et al. [26] and Hafalir et al. [27] have shown that EP reconstruction from solution of the inhomogeneous Helmholtz equation (i.e., without assumption of spatially uniform EPs) is feasible under experimental conditions where the axial component of the RF field can be ignored. In addition to greatly reducing the boundary artifacts, these methods were shown to also reduce the random noise in the reconstructed EPs in a homogenous medium (Fig. 4 of [26] and Fig. 17 of [27]). While more work is needed to better define applicable experimental conditions and characterize systematic errors, advances in methods that explicitly address spatial variation of EPs [20, 26, 27] appear promising towards clinical MREPT. Our work can inform these methods in two ways. First, the minimum uncertainty Laplacian can still be useful since $\nabla^2 B_1$ often appears in the more sophisticated MREPT equations. Second, theoretical SNR of the conventional MREPT can provide an easily accessible reference for evaluation of the SNR of the new methods.

In this work we excluded any nonlinear processing of the input (B_1^+) data [28] or of the reconstructed EP maps (such as a median filter [17]) for noise reduction. Naively, one might think that the SNR gain from the pre- or post-processing steps can be independently added (logarithmically) to the SNR ratios from Eqs. (45,46). However, changes in spatial correlation of the filtered data may complicate such consideration. Investigation of how nonlinear filters can improve the best case SNR of MREPT based on the homogeneous Helmholtz equation could be a relevant subject of a future study.

A major limitation of the present work is the lack of direct experimental validation of the derived SNR equations (Eqs. 45,46). To compensate for this, we presented numerical phantom simulations to support the validity of the key assumptions (Eqs. 15,16) and confirm the soundness of the theoretical development leading to the main results (Eqs. 45,46). We showed that our theory captures many salient features of the SNR behavior of Laplacian-based MREPT that have been reported previously. They include very poor SNR at 1.5T under typical conditions, dramatic SNR gain at higher fields, and quantitative tradeoff (Fig. 5) between better EP localization (favoring a smaller ROI) and SNR (favoring a larger ROI).

In conclusion, we have presented a quantitative relationship between the input and the output noise in MREPT. Despite its limitations, our work provides a useful formula relating the experimental parameters and the SNR of the MREPT in its commonly used form based on the homogeneous Helmholtz equation and a linear Laplacian estimator. Our results can help guide the experimental design and choice of reconstruction parameters in conventional MREPT experiments. Detailed experimental validation and comparison with noise behaviors of other, more sophisticated methods remain as an area of future research.

Acknowledgement

This work was partly supported by the Grant R01CA154433 from the National Institute of Health of USA. The views expressed in this work do not necessarily reflect those of the NIH.

Appendix 1. Derivation of Eqs. (15,16)

We assume that in the ROI in which the electrical properties need to be determined, the spatial variation of B_1^+ is small in magnitude compared to the average B_1^+. That is,

$$\delta_B \equiv \frac{|B_1^+(\vec{r}) - \left\langle B_1^+ \right\rangle|}{|\left\langle B_1^+ \right\rangle|} \ll 1. \quad \text{(A1)}$$

This is reasonable since in most cases MREPT is concerned with determining EPs in an ROI where B_1^+ varies weakly.

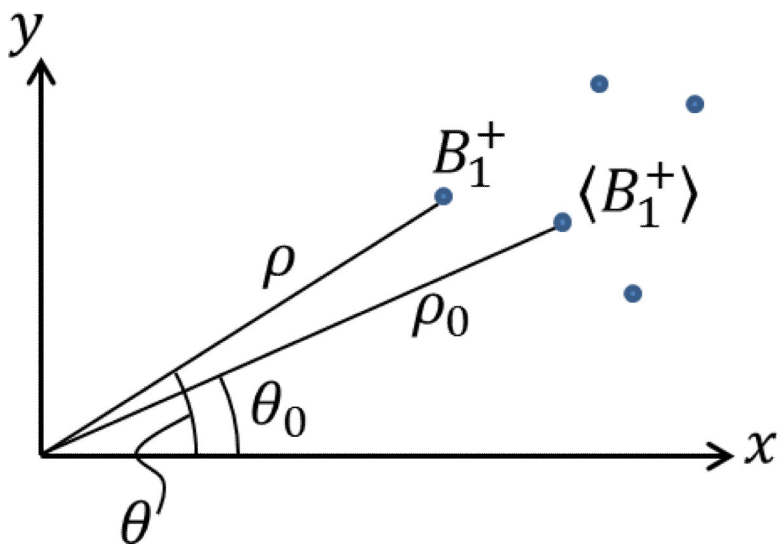

Figure A1.

ROI-averaged $\left\langle B_1^+ \right\rangle$ and a collection of individual voxel B_1^+ in the complex plane.

Figure (A1) illustrates the mean $\left\langle B_1^+ \right\rangle$ and a collection of individual voxel B_1^+ in the complex plane. Let us denote $B_1^+ \left(\vec{r}\right) = \rho e^{i\theta}, \left\langle B_1^+ \right\rangle = \rho_0 e^{i\theta_0}$ in the complex plane. Then the normalized B_1^+ is

$$\frac{B_1^+}{\left\langle B_1^+ \right\rangle} = \frac{\rho}{\rho_0} \cdot \left(cos\left(\theta - \theta_0\right) + i\, sin\left(\theta - \theta_0\right)\right). \quad \text{(A2)}$$

Under the condition Eq. (A1), the real and imaginary parts of the above quantity (r.h.s. of Eq. (A2)) can be approximated to the leading order in δ_B as

$$b_r \approx \frac{\rho}{\rho_0}, \quad \text{(A3)}$$

$$b_i \approx \theta - \theta_0. \quad \text{(A4)}$$

Incidentally, substituting Eqs. (A3,A4) in Eqs. (9,10) (using the definitions of Eqs. (11,12)) leads to the B_1^+ magnitude-only method for ϵ_r and B_1^+ phase-only method for σ calculation [13], respectively. For our purpose, we take the standard deviation of b_r and b_i, with the assumption that the ROI averaged B_1^+ has negligible statistical fluctuation compared to that of B_1^+ at individual voxels: $\Delta\rho_0 \ll \Delta\rho, \Delta\theta_0 \ll \Delta\theta$. This leads to

$$\begin{aligned} \Delta b_r \approx \frac{\Delta\rho}{\rho_0} &= \frac{1}{SNR_{|B_1^+|}} \\ \Delta b_i \approx \Delta\theta &= \Delta\angle B_1^+, \end{aligned}$$

which are Eqs. (15,16).

Appendix 2. Derivation of Eq. (25)

If g_v minimizes Eq. (22) while satisfying Eqs. (23-24), then there exist 10 constants $a_1, a_2, \cdots, a_{10}$ (Lagrange's multipliers) for which the following quantity is minimized unconditionally by g_v:

$$\Phi = \sum_v \left(\frac{1}{2} g_v^2 - g_v \left(a_1 + a_2 x_v + a_3 y_v + a_4 z_v + a_5 x_v y_v + a_6 y_v z_v + a_7 z_v x_v + a_8 x_v^2 + a_9 y_v^2 + a_{10} z_v^2 \right) \right). \quad \text{(A7)}$$

$$\frac{\partial \Phi}{\partial g_v} = 0. \quad \text{(A8)}$$

Eqs. (A7, A8) lead to

$$g_v = a_1 + a_2 x_v + a_3 y_v + a_4 z_v + a_5 x_v y_v + a_6 y_v z_v + a_7 z_v x_v + a_8 x_v^2 + a_9 y_v^2 + a_{10} z_v^2, \quad \text{(A9)}$$

which states that the kernel g_v is a quadratic function of the coordinates. The multipliers are determined by imposing the 10 conditions Eqs. (23-24). We first express Eq. (A9) in terms of the row vectors as

$$\begin{aligned} \mathbf{g} &= a_1 + a_2 \mathbf{x} + a_3 \mathbf{y} + a_4 \mathbf{z} + a_5 \mathbf{xy} + a_6 \mathbf{yz} + a_7 \mathbf{zx} + a_8 \mathbf{x}^2 + a_9 \mathbf{y}^2 + a_{10} \mathbf{z}^2 \\ &= (a_1, a_2, a_3, a_4, a_5, a_6, a_7, a_8, a_9, a_{10})\, \mathbf{F}^T. \end{aligned} \quad \text{(A10)}$$

Next, Eqs. (23-24) can be expressed as

$$\mathbf{gF} = \begin{pmatrix} 0 & 0 & 0 & 0 & 0 & 0 & 0 & 2 & 2 & 2 \end{pmatrix}. \quad \text{(A11)}$$

Substituting Eq. (A10) to Eq. (A11) and solving for the multipliers we get

$$(a_1, a_2, a_3, a_4, a_5, a_6, a_7, a_8, a_9, a_{10}) = \begin{pmatrix} 0 & 0 & 0 & 0 & 0 & 0 & 0 & 2 & 2 & 2 \end{pmatrix} \left(\mathbf{F}^T \mathbf{F} \right)^{-1}. \quad \text{(A12)}$$

Substituting this to Eq. (A10) yields Eq. (25).

References

1. Haacke E, Petropoulos L, Nilges E, Wu D. Extraction of conductivity and permittivity using magnetic resonance imaging. Phys Med Biol. 1991; 36:723–734.

2. Bulumulla, S.; Yeo, T.; Zhu, Y. Direct calculation of tissue electrical parameters from B1 maps. 17th Annual Meeting of ISMRM; Hawaii. 2009; p. 3043
3. Katscher U, Kim DH, Seo JK. Recent progress and future challenges in MR electric properties tomography. Comput Math Methods Med. 2013; 2013:546562. [PubMed: 23573170]
4. Wen H. Noninvasive quantitative mapping of conductivity and dielectric distributions using RF wave propagation effects in high-field MRI. Proc. SPIE 5030, Medical Imaging 2003: Physics of Medical Imaging. 2003:471.
5. Hancu I, Roberts JC, Bulumulla S, Lee SK. On conductivity, permittivity, apparent diffusion coefficient, and their usefulness as cancer markers at MRI frequencies. Magn Reson Med. Jun 19.2014
6. Katscher U, Voigt T, Findeklee C, Vernickel P, Nehrke K, Dossel O. Determination of electric conductivity and local SAR via B1 mapping. IEEE Trans Med Imaging. Sep.2009 28:1365–74. [PubMed: 19369153]
7. van Lier AL, Raaijmakers A, Voigt T, Lagendijk JJ, Luijten PR, Katscher U, van den Berg CA. Electrical properties tomography in the human brain at 1.5, 3, and 7T: a comparison study. Magn Reson Med. Jan.2014 71:354–63. [PubMed: 23401276]
8. Bulumulla, S.; Lee, SK.; Yeo, DTB. Calculation of Electrical Properties from B1+ Maps - A Comparison of Methods. 20th Annual Meeting of ISMRM; Melbourne, Australia. 2012; p. 3469
9. Marques JP, Sodickson DK, Ipek O, Collins CM, Gruetter R. Single acquisition electrical property mapping based on relative coil sensitivities: A proof-of-concept demonstration. Magn Reson Med. Aug 5.2014
10. Lee, S-K.; Bulumulla, SB.; Hancu, I. Efficient tissue permittivity and conductivity mapping using standard MR images. 21st Annual Meeting of ISMRM; Salt Lake City, UT. 2013; p. 462
11. Bulumulla SB, Lee SK, Yeo DT. Conductivity and permittivity imaging at 3.0T. Concepts Magn Reson Part B Magn Reson Eng. Feb 1.2012 41B:13–21. [PubMed: 23599691]
12. van Lier AL, Brunner DO, Pruessmann KP, Klomp DW, Luijten PR, Lagendijk JJ, van den Berg CA. B1(+) phase mapping at 7 T and its application for in vivo electrical conductivity mapping. Magn Reson Med. Feb.2012 67:552–61. [PubMed: 21710613]
13. Voigt T, Katscher U, Doessel O. Quantitative conductivity and permittivity imaging of the human brain using electric properties tomography. Magn Reson Med. Aug.2011 66:456–66. [PubMed: 21773985]
14. Savitzky A, Golay MJE. Smoothing and Differentiation of Data by Simplified Least Squares Procedures. Analytical Chemistry. 1964; 36:1627–1639.
15. Zuo C, Chen Q, Yu Y, Asundi A. Transport-of-intensity phase imaging using Savitzky-Golay differentiation filter - theory and applications. Optics Express. Mar.2013 21:5346–5362. [PubMed: 23482106]
16. Rajagopalan S, Robb R. Image Smoothing with Savitzky-Golay Filters. Proc. SPIE 5029, Medical Imaging 2003: Visualization, Image-Guided Procedures, and Display. 2003:773–781.
17. Katscher, U.; Djamshidi, K.; Voigt, T.; Ivancevic, M.; Abe, H.; Newstead, G.; Keupp, J. Estimation of breast tumor conductivity using parabolic phase fitting. 20th Annual Meeting of ISMRM; Melbourne, Australia. 2012; p. 3482
18. Lee SK, Bulumulla S, Wiesinger F, Sacolick L, Sun W, Hancu I. Tissue electrical property mapping from zero echo-time magnetic resonance imaging. IEEE Trans Med Imaging. Feb.2015 34:541–50. [PubMed: 25312919]
19. Gabriel S, et al. The dielectric properties of biological tissues: III. Parametric models for the dielectric spectrum of tissues. Phys Med Biol. 1996; 41:2271. [PubMed: 8938026]
20. Zhang X, Zhu S, He B. Imaging electric properties of biological tissues by RF field mapping in MRI. IEEE Trans Med Imaging. Feb.2010 29:474–81. [PubMed: 20129847]
21. Mansfield, P.; Morris, PG. NMR Imaging in Biomedicine. Academic Press; New York: 1982.
22. Liu J, Zhang X, Van de Moortele PF, Schmitter S, He B. Determining electrical properties based on B(1) fields measured in an MR scanner using a multi-channel transmit/receive coil: a general approach. Phys Med Biol. Jul 7.2013 58:4395–408. [PubMed: 23743673]
23. Sodickson, DK.; Alon, L.; Deniz, CM.; Brown, R.; Zhang, B.; Wiggins, GC.; Cho, GY.; Eliezer, NB.; Novikov, DS.; Lattanzi, R.; Duan, Q.; Sodickson, LA.; Zhu, Y. Local Maxwell Tomography

Using Transmit-Receive Coil Arrays for Contact-Free Mapping of Tissue Electrical Properties and Determination of Absolute RF Phase. 20th Annual Meeting of ISMRM; Melbourne, Australia. 2012; p. 387

24. Weisskoff RM. Simple measurement of scanner stability for functional NMR imaging of activation in the brain. Magn Reson Med. Oct.1996 36:643–5. [PubMed: 8892220]
25. Friedman L, Glover GH. Report on a multicenter fMRI quality assurance protocol. J Magn Reson Imaging. Jun.2006 23:827–39. [PubMed: 16649196]
26. Liu J, Zhang X, Schmitter S, Van de Moortele PF, He B. Gradient-based electrical properties tomography (gEPT): A robust method for mapping electrical properties of biological tissues in vivo using magnetic resonance imaging. Magn Reson Med. Sep 11.2014
27. Hafalir FS, Oran OF, Gurler N, Ider YZ. Convection-reaction equation based magnetic resonance electrical properties tomography (cr-MREPT). IEEE Trans Med Imaging. Mar.2014 33:777–93. [PubMed: 24595349]
28. Michel E, Hernandez D, Cho MH, Lee SY. Denoising of B(1)(+) field maps for noise- robust image reconstruction in electrical properties tomography. Med Phys. Oct.2014 41:102304. [PubMed: 25281974]

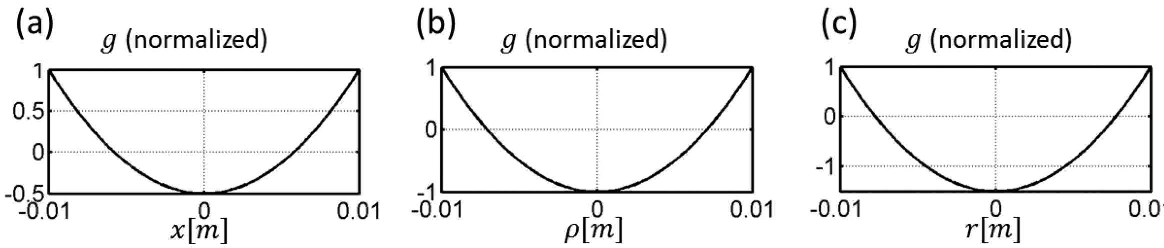

Figure 1.

Functional form of the kernel g as a function of x (a), $\rho \equiv \sqrt{x^2+y^2}$ (b), $r \equiv \sqrt{x^2+y^2+z^2}$ (c), for the 1D, 2D, 3D cases of Table 1 in the continuous limit, respectively. The ROI size is L = 0.02 [m]. Each function is normalized to unity at the boundary.

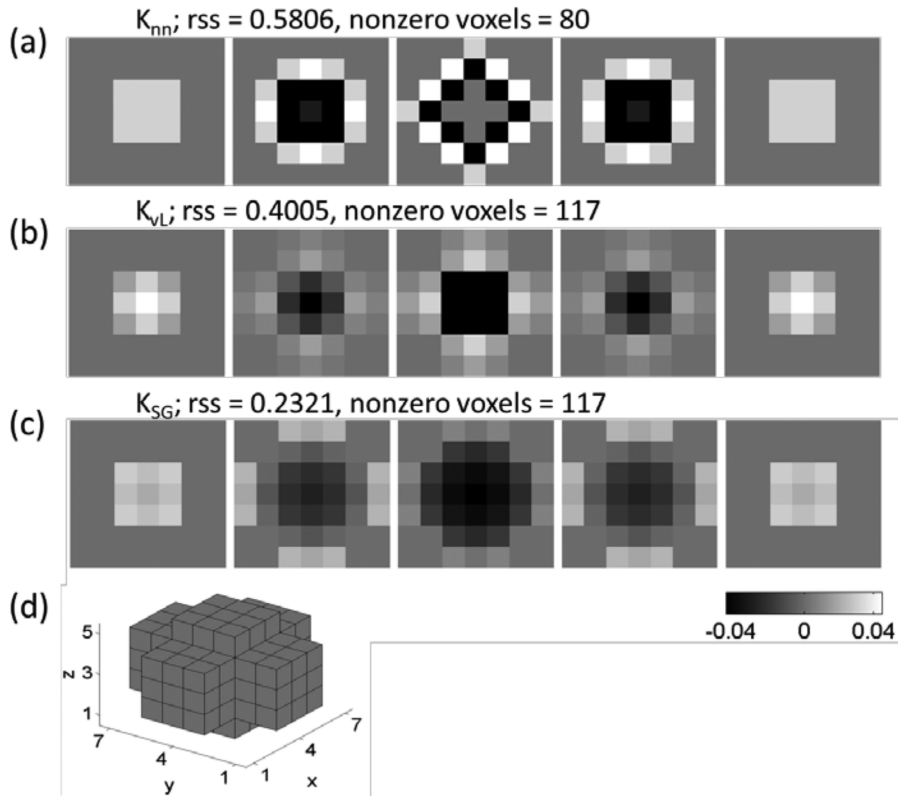

Figure 2.

Comparison of linear Laplacian estimator kernels. Five images correspond to axial slices at $z = 1$ to 5. (a) Kernel that corresponds to averaging all nearest-neighbor Laplacians in the ROI. (b) Kernel used in van Lier et al. [12]. (c) Savitzky-Golay Laplacian kernel. All kernels are defined in the ROI shown in (d) that fits in a $7 \times 7 \times 5$ grid and has $N_{tot} = 117$ voxels. All images have the same grey scale.

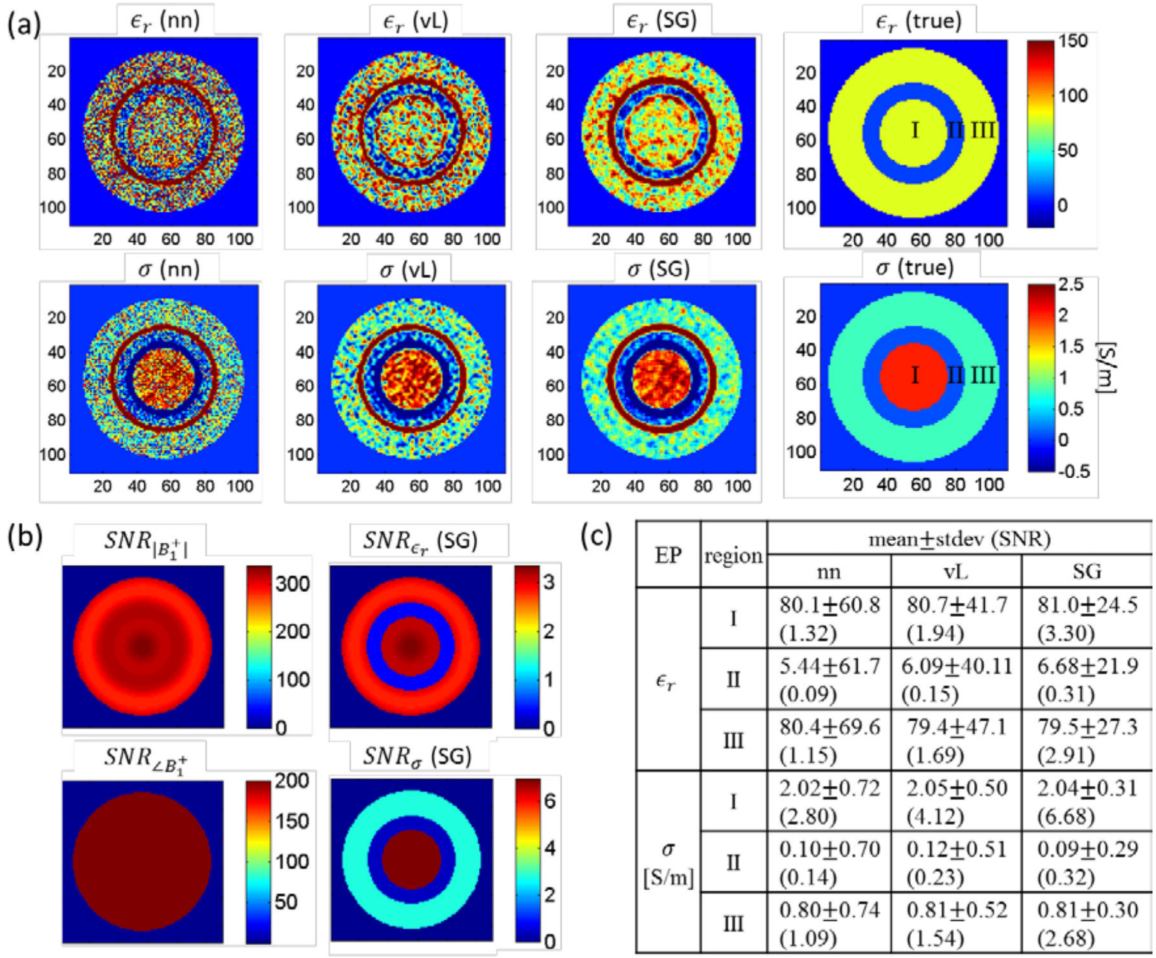

EP	region	mean±stdev (SNR)		
		nn	vL	SG
ϵ_r	I	80.1±60.8 (1.32)	80.7±41.7 (1.94)	81.0±24.5 (3.30)
	II	5.44±61.7 (0.09)	6.09±40.11 (0.15)	6.68±21.9 (0.31)
	III	80.4±69.6 (1.15)	79.4±47.1 (1.69)	79.5±27.3 (2.91)
σ [S/m]	I	2.02±0.72 (2.80)	2.05±0.50 (4.12)	2.04±0.31 (6.68)
	II	0.10±0.70 (0.14)	0.12±0.51 (0.23)	0.09±0.29 (0.32)
	III	0.80±0.74 (1.09)	0.81±0.52 (1.54)	0.81±0.30 (2.68)

Figure 3.

(a) EP maps reconstructed from simulated B_1^+ data on a three-layer cylinder phantom; nn (averaged nearest neighbor), vL (van Lier), and SG (Savitzky-Golay) indicate three different Laplacian kernels of Fig. 2. The last column shows the true ϵ_r and σ. The numbers on the axes label the pixels. (b) SNR of the magnitude and phase of the simulated B_1^+ map (left column), and theoretical SNR maps of EPs for the SG kernel (right column). (c) EP statistics on individual regions (excluding boundary artifacts) for each of the three kernels. SNR, defined as the ratio between the mean and the standard deviation, is shown in parenthesis.

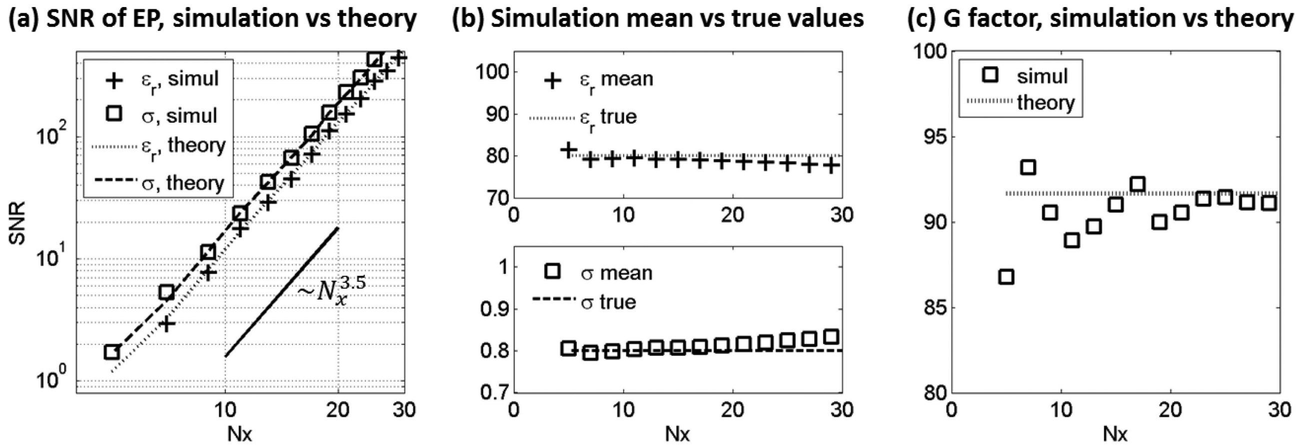

Figure 4.

Numerical simulation on ROI size dependence of the random noise-limited EP SNR. (a) Simulated vs. theoretical SNR in EPs as a function of the linear size (N_x) of the spherical ROI. (b) Simulated mean vs. true EP values. (c) Laplacian noise amplification factor G for a spherical ROI on a discrete grid compared to the continuous-limit value.

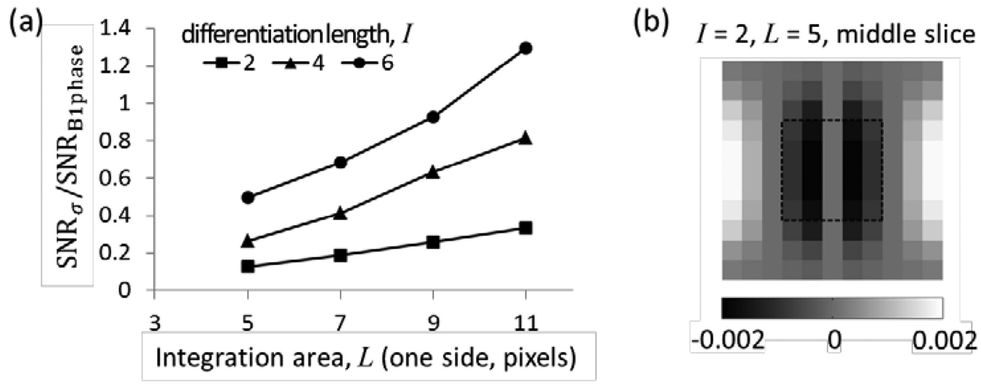

Figure 5.

(a) SNR ratios predicted from the reconstruction kernels of Katscher et al. [6]. *I* is the number of pixels on either side of a target pixel used to compute the derivative. *L* is the length (in pixels) of one side of the square used for B_1 map integration. (b) An example of the kernel with $I = 2$, $L = 5$ on the third of the five slices. The dashed line indicates the $L = 5$ integration area. The kernel values are in unit of (i.e., should be multiplied by) $1/(\Delta x)^2$ where the pixel size is $\Delta x = 1.15$ mm from [6].

Author Manuscript

Author Manuscript

Author Manuscript

Table 1

Minimum uncertainty Laplacian kernels in different ROIs.

ROI	g	*rss*(g)	*G*
1D line with length L	$\frac{30}{N_{tot}L^2}\left(\frac{12}{L^2}\cdot\mathbf{x}^2-\mathbf{1}\right)$	$\frac{12\sqrt{5}}{N_{tot}^{1/2}L^2}$	$12\sqrt{5}=26.83$
2D disc with diameter L	$\frac{96}{N_{tot}L^2}\left(\frac{8}{L^2}\left(\mathbf{x}^2+\mathbf{y}^2\right)-\mathbf{1}\right)$	$\frac{32\sqrt{3}}{N_{tot}^{1/2}L^2}$	$32\sqrt{3}=55.43$
3D sphere with diameter L	$\frac{210}{N_{tot}L^2}\left(\frac{20}{3L^2}\left(\mathbf{x}^2+\mathbf{y}^2+\mathbf{z}^2\right)-\mathbf{1}\right)$	$\frac{20\sqrt{21}}{N_{tot}^{1/2}L^2}$	$20\sqrt{21}=91.65$

Expressions for the 3D sphere case are from Eqs. (37,38,40).

Author Manuscript

Author Manuscript

Author Manuscript

Table 2

A simple case for illustration of SNR in EPs.

parameter	$SNR_{\lvert B_1^+ \rvert}$	$SNR_{\angle B_1^+}$	N_{tot}	L [m]	*dv* [mm^3]	*G* (sphere)
value	100	100	1000	0.02	1.61×1.61×1.61	91.65

dv is the voxel volume.

Table 3

Electrical properties, RF length scales and theoretical random noise-limited MREPT SNR in brain tissue at three different MRI field strengths under the conditions of Table 2.

parameters	unit	grey 1.5T	white 1.5T	grey 3T	white 3T	grey 7T	white 7T
ε_r	1	97.5	67.9	73.6	52.6	60.1	43.8
σ	S/m	0.51	0.29	0.59	0.34	0.69	0.41
$Re(k^2) = \omega^2\varepsilon_0\varepsilon_r\mu_0$	m^{-2}	175	122	527	377	2345	1709
$\lvert Im(k^2)\rvert = \omega\sigma\mu_0$	m^{-2}	257	146	595	343	1624	965
$\lambda = 2\pi / \sqrt{\omega^2\epsilon_0\epsilon_r\mu_0}$	m	0.475	0.570	0.274	0.324	0.130	0.152
$\delta_{skin} = \sqrt{2} / \sqrt{\omega\sigma\mu_0}$	m	0.088	0.117	0.058	0.076	0.035	0.046
SNR_{ε_r}	1	2.4	1.7	7.3	5.2	32.4	23.6
SNR_σ	1	3.5	2.0	8.2	4.7	22.4	13.3

λ, wavelength; δ_{skin}, skin depth.